Computers & Fluids xxx (2012) xxx–xxx

Contents lists available at SciVerse ScienceDirect

Computers & Fluids

journal homepage: www.elsevier.com/locate/compfluid

High-order curvilinear finite elements for axisymmetric Lagrangian hydrodynamics

Veselin A. Dobrev [a], Truman E. Ellis [b], Tzanio V. Kolev [a,*], Robert N. Rieben [c]

[a] Center for Applied Scientific Computing, Lawrence Livermore National Laboratory, United States
[b] Institute for Computational Engineering and Sciences, University of Texas at Austin, United States
[c] Weapons and Complex Integration, B-Division, Lawrence Livermore National Laboratory, United States

ARTICLE INFO

Article history:
Received 23 December 2011
Received in revised form 11 April 2012
Accepted 5 June 2012
Available online xxxx

Keywords:
Axisymmetric problems
Lagrangian hydrodynamics
High-order finite element methods

ABSTRACT

In this paper we present an extension of our general high-order curvilinear finite element approach for solving the Euler equations in a Lagrangian frame [1] to the case of axisymmetric problems. The numerical approximation of these equations is important in a number of applications of compressible shock hydrodynamics and the reduction of 3D problems with axial symmetry to 2D computations provides a significant computational advantage. Unlike traditional staggered-grid hydrodynamics (SGH) methods, which use the so-called "area-weighting" scheme, we formulate our semi-discrete axisymmetric conservation laws directly in 3D and reduce them to a 2D variational form in a meridian cut of the original domain. This approach is a natural extension of the high-order curvilinear finite element framework we have developed for 2D and 3D problems in Cartesian geometry, leading to a rescaled momentum conservation equation which includes new radial terms in the pressure gradient and artificial viscosity forces. We show that this approach exactly conserves energy and we demonstrate via computational examples that it also excels at preserving symmetry in problems with symmetric initial conditions. The results also illustrate that our computational method does not produce spurious symmetry breaking near the axis of rotation, as is the case with many area-weighted approaches.

1. Introduction and motivation

The Euler equations of compressible hydrodynamics describe complex, multi-material, high speed flow and shock wave propagation over general 2D and 3D computational domains. We are interested in Lagrangian numerical methods for these problems, where the equations are discretized and solved on a generally unstructured computational mesh that moves with the fluid velocity. Specifically, the goal of Lagrangian hydrodynamics is to solve the following system of conservation laws:

$$\text{Momentum Conservation}: \quad \rho \frac{dv}{dt} = \nabla \cdot \sigma, \tag{1}$$

$$\text{Mass Conservation}: \quad \frac{1}{\rho}\frac{d\rho}{dt} = -\nabla \cdot v, \tag{2}$$

$$\text{Energy Conservation}: \quad \rho \frac{de}{dt} = \sigma : \nabla v, \tag{3}$$

$$\text{Equation of Motion}: \quad \frac{dx}{dt} = v, \tag{4}$$

$$\text{Equation of State}: \quad \sigma = -EOS(\rho, e)I, \tag{5}$$

which involves the material derivative $\frac{d}{dt}$, the kinematic variables for the fluid velocity v and position x, and the thermodynamic variables for the density ρ, pressure $p = EOS(\rho, e)$ and internal energy e of the fluid [2,3]. The equation of state, EOS, is a constitutive relation which in the simplest case of a polytropic ideal gas with a constant adiabatic index $\gamma > 1$ has the form $p = (\gamma - 1)\rho e$. Our formulation uses a general stress tensor σ in order to accommodate the inclusion of anisotropic tensor artificial viscosity stresses (see Section 3.2) as well as more complex material constitutive relations. We focus on purely Lagrangian methods, and do not consider the other components of a full Arbitrary Lagrangian–Eulerian (ALE) framework in this paper.

Three dimensional simulations of Lagrangian shock hydrodynamics are of great practical importance [3–5], but are also substantially more expensive than 2D calculations. Therefore, for problems with axial symmetry, the reduction of (1)–(5) to computations in a 2D meridian cut provides a significant computational advantage. In previous articles [6,1], we developed a general framework for high-order Lagrangian discretization of the Euler equations using curvilinear finite elements. In this paper, we present the extension of this framework to axisymmetric problems and demonstrate its ability to both conserve energy exactly and maintain symmetry. The realization of both these goals concurrently has proven challenging for many axisymmetric discretization schemes.

Traditional staggered-grid hydrodynamics (SGH) Lagrangian methods for axisymmetric problems have used the "area-weighted"

* Corresponding author.
E-mail address: tzanio@llnl.gov (Tz.V. Kolev).

0045-7930/$ - see front matter © 2012 Elsevier Ltd. All rights reserved.
http://dx.doi.org/10.1016/j.compfluid.2012.06.004

method where the momentum equation is solved in 2D planar coordinates using the "area masses" at nodes while the internal energy equation is solved over the real volumes [7,8]. Generally, this approach does not conserve total energy exactly (unless the compatible approach of [9] is used) and can often lead to incorrect shock speeds, or cause spurious symmetry breaking in the internal energy field near the axis of rotation, leading to non-physical results as illustrated in Figs. 1 and 2. Preservation of physical symmetries is critical for inertial confinement fusion (ICF) simulations as uncertainties in whether non-symmetric results are due to numerical errors or physical processes can limit predictive capability. New compatible approaches have been proposed to address this deficiency [9–14], which have led to significant improvements in energy and symmetry preservation. Other successful methods in this area include the special finite elements proposed in [15,16] and the recent cell-centered hydro approach of [17,18].

In contrast to the above schemes, our finite element numerical method is derived by a faithful reduction of the 3D axisymmetric problem to a 2D variational form in a meridian cut of the domain. This approach conserves total energy exactly by construction. Unlike the area-weighted scheme, it leads to a rescaled momentum conservation equation, which also includes new terms in the pressure gradient and artificial viscosity forces. As in Cartesian coordinates, the high-order finite element approach uses high-order basis function expansions obtained via a high-order mapping from a standard reference element. This enables the use of curvilinear zone geometry and higher order approximations for the fields within a zone.

The remainder of the paper is organized as follows. In Section 2 we introduce notation and recall some basic facts about axisymmetric scalar, vector and tensor fields. These are used in Section 3, where we describe the derivation of our axisymmetric semi-discrete finite element method, followed by discussion of the artificial viscosity, the fully-discrete algorithm and the relation to some classical SGH methods. In Section 4, we present an extensive set of numerical results that demonstrate the robustness of our algorithm with respect to symmetry and energy conservation on a range of challenging axisymmetric problems. Finally, we summarize our experience and draw some conclusions in Section 5.

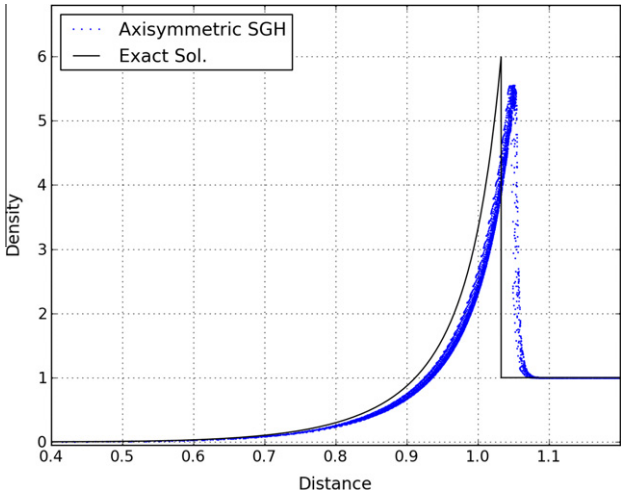

Fig. 1. Scatter plot of the density from a traditional SGH calculation of the spherical Sedov blast wave in axisymmetric mode [19]. The exact solution corresponds to the black line. While the "area-weighted" approach preserves the symmetry of accelerations, the corresponding energy update is not conservative. In this calculation this results in a 6% spurious gain in energy leading to incorrect shock speed and location. These do not improve under mesh refinement.

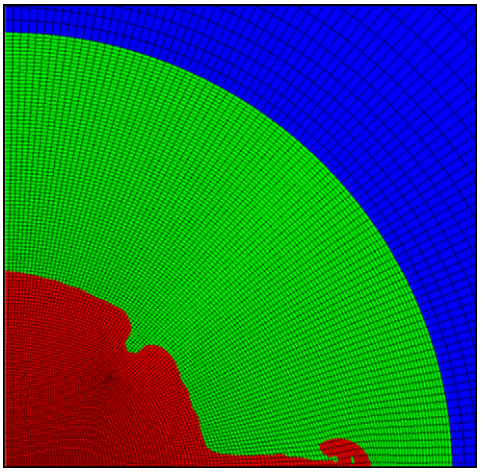

Fig. 2. Example of numerical symmetry breaking in an axisymmetric multi-material inertial confinement fusion (ICF) simulation. This is an ALE calculation where different colors are used to identify the different materials. The jet at the axis of rotation is spurious and does not disappear under mesh refinement.

2. Axisymmetric scalar, vector and tensor fields

In this section we recall some basic facts about axisymmetric fields that will be used in the development of our finite element discretization method in the following section.

We assume that at any given time, the domain Ω occupied by the fluid is a body of revolution, as illustrated in Fig. 3. In cylindrical coordinates (r,θ,z), Ω can be obtained from a "meridian cut" Γ in the r–z plane by a rotation around the axis $r=0$:

$$\Omega = \{(r,\theta,z) : (r,z) \in \Gamma\}.$$

A scalar function f, defined on the axisymmetric domain Ω, is itself called axisymmetric if it is independent of θ, i.e. $f(r,\theta,z) = f(r,z)$, so f is uniquely determined by its values in Γ. If f is given in Cartesian coordinates, it is axisymmetric if and only if

$$\frac{\partial}{\partial\theta} f(r\cos\theta, r\sin\theta, z) = 0,$$

i.e. if f is only spatially varying in the r–z plane

A key property of axisymmetric functions is that their integrals over Ω can be reduced to integrals over Γ:

$$\int_\Omega f(r,\theta,z) = 2\pi \int_\Gamma r f(r,z). \tag{6}$$

The local cylindrical coordinate system vectors at a point (r,θ,z) are given by

$$\vec{e}_r = (\cos\theta, \sin\theta, 0), \quad \vec{e}_\theta = (-\sin\theta, \cos\theta, 0), \quad \vec{e}_z = (0,0,1).$$

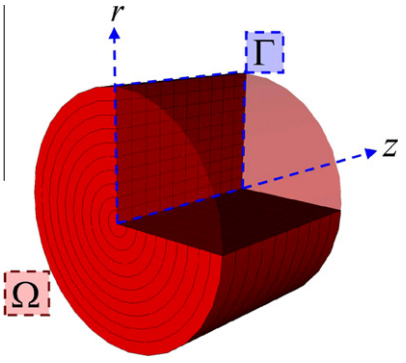

Fig. 3. Schematic depiction of the reduction of a 3D axisymmetric problem to a 2D "meridian cut" in the r–z plane.

Please cite this article in press as: Dobrev VA et al. High-order curvilinear finite elements for axisymmetric Lagrangian hydrodynamics. Comput Fluids (2012), http://dx.doi.org/10.1016/j.compfluid.2012.06.004

Let x and $\xi = (r, \theta, z)$ be the Cartesian and cylindrical coordinates of a point, respectively, so that

$$x = x(\xi) = (r\cos\theta, r\sin\theta, z).$$

The material derivative of ξ can be expressed as

$$\frac{d\xi}{dt} = \frac{\partial \xi}{\partial x}\frac{dx}{dt},$$

which after some simple manipulations can be written as

$$\frac{d}{dt}(r,\theta,z) = \left(v_r, \frac{v_\theta}{r}, v_z\right), \tag{7}$$

where (v_r, v_θ, v_z) are the cylindrical components of the velocity:

$$\frac{dx}{dt} = v = v_r\vec{e}_r + v_\theta\vec{e}_\theta + v_z\vec{e}_z.$$

Identity (7) represents the cylindrical version of the equation of motion (4). Furthermore, using (7) together with the definitions of $\vec{e}_r, \vec{e}_\theta$, and $\vec{e}_z$, the acceleration vector can be expressed as

$$\frac{dv}{dt} = \left(\frac{dv_r}{dt} - \frac{v_\theta^2}{r}\right)\vec{e}_r + \left(\frac{dv_\theta}{dt} + \frac{v_r v_\theta}{r}\right)\vec{e}_\theta + \frac{dv_z}{dt}\vec{e}_z. \tag{8}$$

The material derivative of a scalar field f is given by

$$\frac{df}{dt} = \frac{\partial f}{\partial t} + \frac{\partial f}{\partial \xi}\frac{d\xi}{dt} = \frac{\partial f}{\partial t} + \frac{\partial f}{\partial r}v_r + \frac{\partial f}{\partial \theta}\frac{v_\theta}{r} + \frac{\partial f}{\partial z}v_z,$$

hence if f, v_r, and v_z are axisymmetric then so is $\frac{df}{dt}$.

A vector field v, defined on the axisymmetric domain Ω, is called axisymmetric if

$$v = v_r(r,z)\vec{e}_r + v_\theta(r,z)\vec{e}_\theta + v_z(r,z)\vec{e}_z,$$

i.e. if v remains invariant under arbitrary rotation around the axis $r = 0$. This is the most general axial symmetry assumption for a vector field which requires the use of the additional (compared to a 2D method) velocity component v_θ and is generally more complex to handle. Therefore, here we consider the more standard additional assumption that $v_\theta \equiv 0$, i.e. axisymmetric vector fields without components in the normal direction of the meridian cut. With this assumption the equation of motion (7) and the left hand side of the momentum conservation equation (1), as well as (8), simplify and become identical to the 2D case in the meridian cut Γ.

The gradient operator in cylindrical coordinates is given by

$$\nabla_{rz} f = \frac{\partial f}{\partial r}\vec{e}_r + \frac{1}{r}\frac{\partial f}{\partial \theta}\vec{e}_\theta + \frac{\partial f}{\partial z}\vec{e}_z. \tag{9}$$

Therefore, $\nabla_{rz} f$ is axisymmetric if and only if f is. In this case, the formula simplifies to

$$\nabla_{rz} f = \frac{\partial f}{\partial r}\vec{e}_r + \frac{\partial f}{\partial z}\vec{e}_z,$$

which is just the regular 2D gradient in Γ. Note that this property is one of the motivating factors for using area-weighting schemes, as it implies that gradient operators are unchanged in axisymmetric coordinates.

The divergence in cylindrical coordinates is more complicated:

$$\nabla_{rz}\cdot v = \frac{\partial v_r}{\partial r} + \frac{1}{r}\frac{\partial v_\theta}{\partial \theta} + \frac{\partial v_z}{\partial z} + \frac{v_r}{r}, \tag{10}$$

but $\nabla_{rz}\cdot v$ is still axisymmetric, provided that v is. In this case, the formula simplifies to

$$\nabla_{rz}\cdot v = \frac{\partial v_r}{\partial r} + \frac{\partial v_z}{\partial z} + \frac{v_r}{r},$$

which has an extra term compared to the regular 2D divergence in Γ.

The gradient of the axisymmetric vector function $v = v_r(r,z)\vec{e}_r + v_z(r,z)\vec{e}_z$ can be written as

$$\begin{aligned}\nabla_{rz} v &= \vec{e}_r \otimes \frac{\partial v}{\partial r} + \frac{1}{r}\vec{e}_\theta \otimes \frac{\partial v}{\partial \theta} + \vec{e}_z \otimes \frac{\partial v}{\partial z}\\ &= \frac{\partial v_r}{\partial r}\vec{e}_r\otimes\vec{e}_r + \frac{\partial v_z}{\partial r}\vec{e}_r\otimes\vec{e}_z + \frac{v_r}{r}\vec{e}_\theta\otimes\vec{e}_\theta\\ &\quad + \frac{\partial v_r}{\partial z}\vec{e}_z\otimes\vec{e}_r + \frac{\partial v_z}{\partial z}\vec{e}_z\otimes\vec{e}_z,\end{aligned}$$

so the matrix form of the gradient in the $z - r - \theta$ ordering is

$$\nabla_{rz} v = \begin{pmatrix} \frac{\partial v_z}{\partial z} & \frac{\partial v_r}{\partial z} & 0\\ \frac{\partial v_z}{\partial r} & \frac{\partial v_r}{\partial r} & 0\\ 0 & 0 & \frac{v_r}{r}\end{pmatrix} = \begin{pmatrix} \nabla_{2d} v & 0\\ 0 & \frac{v_r}{r}\end{pmatrix}. \tag{11}$$

A tensor field σ is axisymmetric if its components in the local cylindrical basis are independent of θ and have the form

$$\sigma = \begin{pmatrix} \sigma_{zz} & \sigma_{zr} & 0\\ \sigma_{rz} & \sigma_{rr} & 0\\ 0 & 0 & \sigma_{\theta\theta}\end{pmatrix} = \begin{pmatrix} \sigma_{2d} & 0\\ 0 & \sigma_{\theta\theta}\end{pmatrix}.$$

Since the local cylindrical basis is orthonormal, the contraction (or double dot product) of σ and $\nabla_{rz} v$ is given by

$$\sigma : \nabla_{rz} v = \sigma_{2d} : \nabla_{2d} v + \sigma_{\theta\theta}\frac{v_r}{r},$$

which is a scalar axisymmetric field, i.e. it is independent of θ.

3. Finite element discretization

In this section we derive and discuss a finite element-based numerical approximation scheme for the Euler equations (1)–(5) in axisymmetric form. The presentation follows the finite element form of the general semi-discrete Lagrangian discretization method from [1], to which we refer for additional details.

3.1. Semi-discrete formulation

We first discuss the semi-discrete axisymmetric method, which is concerned only with the spatial approximation of the continuum equations. The fully-discrete methods that incorporate time discretization will be presented in Section 3.3.

Let $\Omega(t)$ be the continuous 3D axisymmetric medium (fluid or elastic body) which is deforming in time according to (1)–(5) starting from an initial configuration at time $t = t_0$. Let $\Gamma(t)$ be the corresponding meridian cut, as discussed in Section 2. Following [1], we introduce a 2D finite element mesh on $\widetilde{\Gamma} \equiv \Gamma(t_0)$ with zones (or elements) $\{\Gamma_z(t_0)\}$. This also induces a decomposition of $\widetilde{\Omega} \equiv \Omega(t_0)$ into toroidal zones $\{\Omega_z(t_0)\}$ obtained by revolution of the 2D mesh elements around the axis $r = 0$ in cylindrical coordinates:

$$\Omega_z(t_0) = \{(r,\theta,z) : (r,z) \in \Gamma_z(t_0)\}. \tag{12}$$

A main feature of our approach is that the finite element mesh is described through the locations of high-order particles (or control points) that are tracked by the semi-discrete algorithm. This results in curvilinear zones that can better represent the naturally developing curvature in the flow. Specifically, the current position at time t, $x = (r,z) \in \Gamma(t)$, corresponding to a particle at an initial position $\tilde{x} = (\tilde{r},\tilde{z}) \in \widetilde{\Gamma}$ is discretized using the expansion

$$x(\tilde{x},t) = \sum_{i=1}^{N_v}\mathbf{x}_i(t)w_i(\tilde{x}) = \mathbf{x}(t)^{\mathrm{T}}\mathbf{w}(\tilde{x}), \tag{13}$$

where $\mathbf{x}(t)$ is an unknown time-dependent vector of coefficients in the kinematic basis $\{w_i\}_{i=1}^{N_v}$, and $\mathbf{w}$ is a column vector of all the basis

Please cite this article in press as: Dobrev VA et al. High-order curvilinear finite elements for axisymmetric Lagrangian hydrodynamics. Comput Fluids (2012), http://dx.doi.org/10.1016/j.compfluid.2012.06.004

functions $\{w_i\}$. The kinematic basis functions are defined through Cartesian products of nodal finite element basis functions $\{\hat{\eta}_i\}_{i=1}^{N_v}$ defined on a standard reference zone $\widehat{\Gamma}_z$, which is the unit square in all cases considered in this paper. The curvilinear zones at time t are then reconstructed as

$$\Gamma_z(t) = \{x = \Phi_z(\hat{x}, t) : \hat{x} \in \widehat{\Gamma}_z\}, \tag{14}$$

where Φ_z is the parametric mapping from the reference element

$$\Phi_z(\hat{x}, t) = \sum_{i=1}^{N_v} x_{z,i}(t)\, \hat{\eta}_i(\hat{x}). \tag{15}$$

We denote the Jacobian of this mapping by $\mathbf{J}_z = \nabla_{\hat{x}} \Phi_z$.

Note that the same nodal basis is used for discretization of both the position and the velocity fields, so each component of a $w_i|_{\Gamma_z}$ corresponds to a mapped basis function, $\hat{\eta}_p \circ \Phi_z^{-1}$, for some index p (the index of the particle i on the reference element). The discrete velocity field corresponding to the motion (13) is given by

$$v(\tilde{x}, t) = \sum_i \frac{d\mathbf{x}_i}{dt}(t) w_i(\tilde{x}) = \mathbf{v}(t)^{\mathrm{T}} \mathbf{w}(\tilde{x}), \quad \text{i.e. } \mathbf{v} = \frac{d\mathbf{x}}{dt}$$

in agreement with (4) and (7).

We next discuss the reduction of the mass conservation law, which is fundamental in the Lagrangian framework. We start from the following equivalent form of (2): let $\Omega'(t)$ be the revolution of an arbitrary set $\Gamma'(t) \subseteq \Gamma(t)$, then mass conservation postulates that

$$\int_{\Omega'(t)} \rho(t) = \int_{\Omega'(t_0)} \rho(t_0),$$

i.e. the total mass in any axisymmetric volume $\Omega'(t)$ at time t equals the initial mass at time t_0. Due to (6), this is equivalent to

$$2\pi \int_{\Gamma'(t)} r\rho(t) = 2\pi \int_{\Gamma'(t_0)} r\rho(t_0).$$

Since $\Gamma'(t)$ is arbitrary, we can reduce this further using a change of variables to $\widetilde{\Gamma} \equiv \Gamma(t_0)$:

$$r(t)\rho(t)|\widetilde{J}(t)| = r(t_0)\rho(t_0),$$

where $|\widetilde{J}(t)|$ is the determinant of the Jacobian of the mapping $x = x(\tilde{x}, t)$. In the finite element setting, the above equality can be written as

$$r(t)\rho(t)|\mathbf{J}_z(t)| = r(t_0)\rho(t_0)|\mathbf{J}_z(t_0)|. \tag{16}$$

We refer to the above semi-discrete principle as *strong mass conservation*, and we note that the only difference between this axisymmetric version and the Cartesian version from (4.8) in [1] is the extra r term on both sides of (16). Strong mass conservation allows us to express the density at time t as a (non-polynomial) function of the original density, effectively eliminating ρ from the semi-discrete algorithm, and can be viewed as a high order generalization of zonal mass conservation. Since (16) is not well-defined on the axis of rotation, we make sure to only apply it at points where $r \neq 0$.

We now focus on the derivation of the axisymmetric form of the momentum conservation equation. Multiplying (1) by a revolved test function w_j and integrating by parts, we get the weak variational formulation

$$\int_{\Omega(t)} \rho \frac{dv}{dt} \cdot w_j = -\int_{\Omega(t)} \sigma : \nabla w_j + \int_{\partial\Omega(t)} n \cdot \sigma \cdot w_j, \tag{17}$$

where n is the outward pointing unit normal vector of the surface $\partial\Omega(t)$. Assuming the boundary integral term vanishes and applying (6) we obtain

$$2\pi \int_{\Gamma(t)} r\rho \frac{dv}{dt} \cdot w_j = -2\pi \int_{\Gamma(t)} r\sigma_{rz} : \nabla_{rz} w_j. \tag{18}$$

Using (11) and contraction of axisymmetric tensors, we can write (18) in the form

$$\int_{\Gamma(t)} r\rho \frac{dv}{dt} \cdot w_j = -\int_{\Gamma(t)} r\left(\sigma_{2d} : \nabla_{2d} w_j\right) + \sigma_{\theta\theta}(w_j)_r,$$

where σ_{2d} and ∇_{2d} are just the regular 2D stress and gradient tensors in Γ and $(w_j)_r$ denotes the radial component of the vector basis function w_j. This can be viewed as a perturbation of the Cartesian case, where the weak variational formulation reads

$$\int_{\Gamma(t)} \rho \frac{dv}{dt} \cdot w_j = -\int_{\Gamma(t)} \sigma_{2d} : \nabla_{2d} w_j.$$

We emphasize that even though the two versions are similar, they are not the same due to the r weighing of the integrals and the extra stress term $\sigma_{\theta\theta}$ (which includes the pressure and the artificial stress: $\sigma_{\theta\theta} = -p + \sigma_{a,\theta\theta}$) on the right-hand side of the axisymmetric case. This is in contrast to the "area-weighting" scheme which essentially uses the Cartesian form in axisymmetric computations. While our approach is more faithful to the original 3D equations on Ω, we do not automatically inherit the symmetry-preservation properties of the Cartesian form. Nevertheless, we do observe good symmetry preservation in practice as illustrated in Section 4.

Let $\mathbf{M}_v$ be the *axisymmetric kinematic mass matrix* (we skip the 2π factor)

$$\mathbf{M}_v = \int_{\Gamma(t)} r\rho \mathbf{w}\mathbf{w}^{\mathrm{T}}, \tag{19}$$

where we have defined the basis $\mathbf{w}(t)$ by moving $\mathbf{w}(t_0)$ according to the Lagrangian motion (13). This means that $\frac{d\mathbf{w}}{dt} = 0$, which together with (16) implies

$$\frac{d\mathbf{M}_v}{dt} = 0,$$

i.e., the kinematic mass matrix is independent of time. This is an important feature of our approach.

With the above notation, we can write our semi-discrete momentum conservation briefly as

$$\mathbf{M}_v \frac{d\mathbf{v}}{dt} = -\int_{\Gamma(t)} r\sigma_{rz} : \nabla_{rz} \mathbf{w}. \tag{20}$$

To discretize the energy conservation law, we introduce a thermodynamic approximation space with basis $\{\phi_i\}_{j=1}^{N_\varepsilon}$ which is analogous to the kinematic basis, except that it is discontinuous (we make this choice due to the local nature of the equation of state). The internal energy is then approximated as

$$e(\tilde{x}, t) = \sum_j \mathbf{e}_j(t)\phi_j(\tilde{x}) = \mathbf{e}(t)^{\mathrm{T}} \boldsymbol{\phi}(\tilde{x}),$$

where $\mathbf{e}(t)$ is an unknown time-dependent vector of size N_ε and $\boldsymbol{\phi}(\tilde{x})$ is a column vector of all the basis functions $\{\phi_j\}_{j=1}^{N_\varepsilon}$.

The weak variational formulation of the energy conservation Eq. (3) is obtained by multiplying it by ϕ_i and integrating over the domain $\Omega(t)$:

$$\int_{\Omega(t)} \left(\rho \frac{de}{dt}\right) \phi_i = \int_{\Omega(t)} (\sigma : \nabla v)\, \phi_i. \tag{21}$$

Using (6), this reads

$$2\pi \int_{\Gamma(t)} r\left(\rho \frac{de}{dt}\right) \phi_i = 2\pi \int_{\Gamma(t)} r(\sigma_{rz} : \nabla_{rz} v)\, \phi_i,$$

which can be written briefly as

Please cite this article in press as: Dobrev VA et al. High-order curvilinear finite elements for axisymmetric Lagrangian hydrodynamics. Comput Fluids (2012), http://dx.doi.org/10.1016/j.compfluid.2012.06.004

$$\mathbf{M}_{\mathcal{E}} \frac{d\mathbf{e}}{dt} = \int_{\Gamma(t)} r(\sigma_{rz} : \nabla_{rz} v)\, \boldsymbol{\phi}, \tag{22}$$

where $\mathbf{M}_{\mathcal{E}}$ is the *axisymmetric thermodynamic mass matrix*

$$\mathbf{M}_{\mathcal{E}} \equiv \int_{\Gamma(t)} r\rho\boldsymbol{\phi}\boldsymbol{\phi}^{\mathrm{T}}. \tag{23}$$

Similarly to $\mathbf{M}_{\mathcal{V}}$, this matrix is independent of time.

We finally introduce the so-called *axisymmetric force matrix* that connects the kinematic and thermodynamic spaces:

$$\mathbf{F}_{ij} = \int_{\Gamma(t)} r(\sigma_{rz} : \nabla_{rz} w_i)\phi_j. \tag{24}$$

This allows us to summarize our axisymmetric semi-discrete Lagrangian conservation laws in the following simple form:

$$\text{Momentum Conservation}: \quad \mathbf{M}_{\mathcal{V}} \frac{d\mathbf{v}}{dt} = -\mathbf{F} \cdot \mathbf{1}, \tag{25}$$

$$\text{Energy Conservation}: \quad \mathbf{M}_{\mathcal{E}} \frac{d\mathbf{e}}{dt} = \mathbf{F}^{\mathrm{T}} \cdot \mathbf{v}, \tag{26}$$

$$\text{Equation of Motion}: \quad \frac{d\mathbf{x}}{dt} = \mathbf{v}. \tag{27}$$

Here $\mathbf{1}$ is a vector representing the constant one in the thermodynamic basis $\{\phi_i\}$.

The above semi-discrete form is identical to the one from the 2D Cartesian case [1], with the only differences being the r-scaling in the integrals and the extra terms in the force matrix. In particular, the time independence of the mass matrices and the compatible right-hand sides of (25) and (26) imply that the above semi-discrete scheme will conserve total energy exactly on a semi-discrete level. The proof of this fact can be found in [1]; we present it below for completeness.

The change in the total energy

$$E(t) = \int_{\Omega(t)} \rho \frac{|v|^2}{2} + \rho e \tag{28}$$

can be expressed in the semi-discrete settings using (6) as:

$$\frac{dE}{dt} = 2\pi \frac{d}{dt}\left(\frac{1}{2}\mathbf{v} \cdot \mathbf{M}_{\mathcal{V}} \cdot \mathbf{v} + \mathbf{1} \cdot \mathbf{M}_{\mathcal{E}} \cdot \mathbf{e}\right).$$

Since $\mathbf{M}_{\mathcal{V}}, \mathbf{M}_{\mathcal{E}}$ and $\mathbf{1}$ are independent of time and $\mathbf{M}_{\mathcal{V}}$ is symmetric, we have

$$\frac{1}{2\pi}\frac{dE}{dt} = \mathbf{v} \cdot \mathbf{M}_{\mathcal{V}} \cdot \frac{d\mathbf{v}}{dt} + \mathbf{1} \cdot \mathbf{M}_{\mathcal{E}} \cdot \frac{d\mathbf{e}}{dt}.$$

Substituting Eqs. (25) and (26) in the right hand side we get

$$\frac{1}{2\pi}\frac{dE}{dt} = -\mathbf{v} \cdot \mathbf{F} \cdot \mathbf{1} + \mathbf{1} \cdot \mathbf{F}^{\mathrm{T}} \cdot \mathbf{v} = 0,$$

where the last equality follows from the identity $\mathbf{x} \cdot \mathbf{A} \cdot \mathbf{y} = \sum_{ij} \mathbf{x}_i \mathbf{A}_{ij} \mathbf{y}_j = \mathbf{y} \cdot \mathbf{A}^{\mathrm{T}} \cdot \mathbf{x}$. Thus, we can conclude that the total energy remains constant in time.

Remark 1. As an alternative to the more explicit Γ-based perspective presented in this section, one can also consider the direct discretization of the 3D domain Ω using the rotated versions of the finite element mesh, cf. (12), as well as the kinematic and thermodynamic spaces. Though the resulting 3D approximation spaces $\mathcal{V}$ and $\mathcal{E}$ are not of finite element type, they are finite dimensional, so the abstract semi-discrete Lagrangian variational formulation from Section 3 in [1] still applies. In particular, we can conclude that the above semi-discrete equations (with integrals computed e.g. by reduction to the meridian cut) exactly satisfy the properties of mass, momentum and energy conservation as well as the geometric conservation law, based on Theorem 3.1 from [1].

3.2. Axisymmetric tensor artificial viscosity

In this section we briefly outline the modifications to the tensor artificial viscosity term from Section 6 in [1] which are necessary for the axisymmetric case. The changes are minor, so we simply outline them for the specific case of the artificial stress type 2,

$$\sigma_{a,2} = \mu\varepsilon(v). \tag{29}$$

Similar considerations apply to the other viscosity types considered in [1].

First, we note that the symmetrized gradient of the velocity field,

$$\varepsilon(v) \equiv \frac{1}{2}(\nabla v + v\nabla),$$

has the following form in the axisymmetric case (using the $z - r - \theta$ ordering from Section 2

$$\varepsilon(v) = \begin{pmatrix} \varepsilon_{2d}(v) & 0 \\ 0 & \frac{v_r}{r} \end{pmatrix}$$

where $\varepsilon_{2d}(v)$ is simply the symmetrized gradient in Γ. There is no problem with division by zero in the $\theta\theta$ component of the stress tensor, since when it is used in the force computations of (24), $\varepsilon(v)_{\theta\theta}$ generates the extra term $\frac{v_r}{r}(w_i)_r\phi_j$, which is zero on $r = 0$ due to the boundary conditions of symmetry in the kinematic space. Furthermore, $\sigma_{a,2}$ is only being evaluated at Gaussian quadrature points, which all have $r \neq 0$.

The coefficient μ in (29) is based on a "shock direction" vector s, which we assume to lie in the meridian cut plane Γ, i.e. we ignore the $\vec{e}_\theta$ eigenvector of $\varepsilon(v)$ and compute s only from $\varepsilon_{2d}(v)$ (same as in 2D).

The overall form of the directional viscosity coefficient is

$$\mu_s = \tilde{\rho}\left[q_2\psi_2\ell_s^2|\Delta_s v| + q_1\psi_0\psi_1\ell_s c_s\right]$$

where we use the axisymmetric strong mass conservation to compute $\tilde{\rho}$:

$$\tilde{\rho} = \rho(t_0)\frac{r(t_0)|\mathbf{J}_z(t_0)|}{r(t)|\mathbf{J}_z(t)|}.$$

The measure of compression $|\Delta_s v|$ and the directional length scale ℓ_s are the same as in 2D because s lies in Γ. The only other difference is in the vorticity/compression measure, which incorporates the rz divergence of (10)

$$\psi_0 = \frac{|\nabla_{2d} \cdot v + v_r/r|}{\sqrt{\|\nabla_{2d} v\|^2 + |v_r/r|^2}}.$$

Again, division by zero on the axis $r = 0$ does not arise, since the Gaussian quadrature points in which ψ_0 is being evaluated are in the interior of the computational zones.

3.3. Fully-discrete method

Let $\{t_n\}_{n=0}^{N_t}$ be different moments in time and denote $\Gamma^n \equiv \Gamma(t_n)$ and $\Omega^n \equiv \Omega(t_n)$. We use a superscript n to identify the quantities associated with t_n.

As in [1], let $Y = (\mathbf{v}; \mathbf{e}; \mathbf{x})$ be a vector of the hydrodynamic state variables. Our semi-discrete conservation equations then are:

$$\frac{dY}{dt} = \mathcal{F}(Y, t),$$

Please cite this article in press as: Dobrev VA et al. High-order curvilinear finite elements for axisymmetric Lagrangian hydrodynamics. Comput Fluids (2012), http://dx.doi.org/10.1016/j.compfluid.2012.06.004

where

$$\mathcal{F}(Y,t) = \begin{pmatrix} \mathcal{F}_v(\mathbf{v},\mathbf{e},\mathbf{x}) \\ \mathcal{F}_e(\mathbf{v},\mathbf{e},\mathbf{x}) \\ \mathcal{F}_x(\mathbf{v},\mathbf{e},\mathbf{x}) \end{pmatrix} = \begin{pmatrix} -\mathbf{M}_{\mathcal{V}}^{-1}\mathbf{F}\cdot\mathbf{1} \\ \mathbf{M}_{\mathcal{E}}^{-1}\mathbf{F}^{\mathrm{T}}\cdot\mathbf{v} \\ \mathbf{v} \end{pmatrix}$$

We can apply standard high-order time integration solvers to the above system of nonlinear ODEs, including variants of explicit Runge–Kutta methods, such as RK4, or the RK2-Average scheme from Section 7.1 in [1]:

$$\mathbf{v}^{n+\frac{1}{2}} = \mathbf{v}^n - (\Delta t/2)\,\mathbf{M}_{\mathcal{V}}^{-1}\mathbf{F}^n\cdot\mathbf{1},$$

$$\mathbf{e}^{n+\frac{1}{2}} = \mathbf{e}^n + (\Delta t/2)\,\mathbf{M}_{\mathcal{E}}^{-1}(\mathbf{F}^n)^{\mathrm{T}}\cdot\mathbf{v}^{n+\frac{1}{2}},$$

$$\mathbf{x}^{n+\frac{1}{2}} = \mathbf{x}^n + (\Delta t/2)\,\mathbf{v}^{n+\frac{1}{2}},$$

$$\mathbf{v}^{n+1} = \mathbf{v}^n - \Delta t\,\mathbf{M}_{\mathcal{V}}^{-1}\mathbf{F}^{n+\frac{1}{2}}\cdot\mathbf{1},$$

$$\mathbf{e}^{n+1} = \mathbf{e}^n + \Delta t\,\mathbf{M}_{\mathcal{E}}^{-1}(\mathbf{F}^{n+\frac{1}{2}})^{\mathrm{T}}\cdot\bar{\mathbf{v}}^{n+\frac{1}{2}},$$

$$\mathbf{x}^{n+1} = \mathbf{x}^n + \Delta t\,\bar{\mathbf{v}}^{n+\frac{1}{2}},$$

where $\mathbf{F}^n = \mathbf{F}(Y^n)$ and $\bar{\mathbf{v}}^{n+\frac{1}{2}} = (\mathbf{v}^n + \mathbf{v}^{n+1})/2$. This choice has the attractive property that it conserves the discrete total energy exactly [1] and is the default time integrator in the numerical experiments in Section 4.

Our automatic time-step control for determining Δt is based on the density, sound speed, viscosity coefficient and minimal singular values of the Jacobian $\mathbf{J}_z$, which do not require any modifications in the axisymmetric case.

3.4. Relation to SGH methods

In this section we describe several connections between our finite element framework and some classical discretization schemes under additional discretization assumptions.

As in Section 5.1 of [1], we first consider the evaluation of the axisymmetric kinematic mass matrix in the case of a piecewise bilinear kinematic approximation and a single point quadrature rule with mass lumping. This produces a diagonal matrix, with "nodal masses"

$$m_n = \sum_{\Gamma_z \ni n} \frac{1}{4} m_z, \quad \text{where } m_z = r_z \rho_z |\Gamma_z|. \tag{30}$$

Here, $|\Gamma_z|$ is the area of the zone, r_z and ρ_z denote the values of r and the density in the zone center, and the sum is taken over all zones containing a fixed node (vertex) n.

In our algorithm, the zonal density ρ_z is computed through the strong mass conservation principle (16) at the center of the zone Ω_z, i.e.

$$r_z(t)\rho_z(t)|\Gamma_z(t)| = r_z(t_0)\rho_z(t_0)|\Gamma_z(t_0)|. \tag{31}$$

This ensures that the nodal (kinematic) and zonal (thermodynamic) masses m_n and m_z remain constant in time.

Note that we can write (30) in the form

$$m_n = \frac{1}{4}\sum_{\Gamma_z \ni n} r_z m_z^{2d}, \quad \text{where } m_z^{2d} = \rho_z |\Gamma_z|,$$

which is an r-weighted version of the two-dimensional SGH nodal masses from [7].

Applying the same one point quadrature rule in the computation of the force representing the right-hand side of the momentum equation we get (analogously to [1])

$$f_n = \sum_{\Gamma_z \ni n} \mathbf{f}_{z,n}, \tag{32}$$

where the axisymmetric *corner force* vector $\mathbf{f}_{z,n}$ relates to the 2D HEMP corner forces $\mathbf{f}_{z,n}^{2d}$ of [7] as follows:

$$\mathbf{f}_{z,n} = r_z \mathbf{f}_{z,n}^{2d} + \frac{p_z|\Gamma_z|}{4}\begin{pmatrix} 0 \\ 1 \end{pmatrix}_{z-r}, \tag{33}$$

i.e. $\mathbf{f}_{z,n}$ is an r-weighted version of $\mathbf{f}_{z,n}^{2d}$ plus an extra pressure term in its r component.

To summarize, under the specified simplifying assumptions, our axisymmetric momentum equation for the nodal accelerations a_n reads

$$m_n a_n = f_n, \tag{34}$$

or

$$\frac{1}{4}\left(\sum_{\Gamma_z \ni n} r_z m_z^{2d}\right) a_n = \sum_{\Gamma_z \ni n} r_z \mathbf{f}_{z,n}^{2d} + \frac{p_z|\Gamma_z|}{4}\begin{pmatrix} 0 \\ 1 \end{pmatrix},$$

which is similar to, but differs from the "area-weighted" (Cartesian) version

$$\frac{1}{4}\left(\sum_{\Gamma_z \ni n} m_z^{2d}\right) a_n^{2d} = \sum_{\Omega_z \ni n} \mathbf{f}_{z,n}^{2d}.$$

We next discuss the discretization of the internal energy equation for the specific case of a piece-wise constant thermodynamic basis. In the Wilkins approach, [7] the rz velocity divergence in the center of a zone is approximated through the rate of change of its revolved volume

$$\frac{1}{|\Omega_z(t)|}\frac{d|\Omega_z(t)|}{dt} = \nabla\cdot v. \tag{35}$$

This formula is related to the so-called geometric conservation law,

$$\frac{d|\Omega(t)|}{dt} = \int_{\Omega(t)} \nabla\cdot v, \tag{36}$$

but we remark that unlike the Cartesian case, (35) is only an approximation to, and not equivalent with (36).

In the general *compatible hydro* approach [20,9,21], the right-hand side of the energy equation is evaluated through the corner forces computed in the momentum equation:

$$m_z \frac{de_z}{dt} = -\sum_{n\in\Gamma_z} \mathbf{f}_{z,n}\cdot v_n. \tag{37}$$

It is straightforward to check that we recover the above formula under the specified simplifying assumptions, with m_z defined in (30) and v_n denoting the velocity vector at node n.

Finally, we comment that the simplified SGH-like scheme based on (34) and (37) with the definitions (30)–(33) inherits the exact total energy conservation property, in the sense that

$$\frac{d}{dt}\left(\sum_n m_n \frac{|v_n|^2}{2} + \sum_{\Gamma_z} m_z e_z\right) = 0.$$

Indeed, since the nodal masses do not change, we have

$$\frac{d}{dt}\sum_n m_n \frac{|v_n|^2}{2} = \sum_n m_n a_n\cdot v_n = \sum_n f_n\cdot v_n.$$

On the other hand, (32) and the constant zonal masses imply after interchanging the summation order

$$\sum_n f_n\cdot v_n = \sum_{\Gamma_z}\sum_{n\in\Gamma_z} \mathbf{f}_{z,n}\cdot v_n = -\frac{d}{dt}\sum_{\Gamma_z} m_z e_z,$$

which completes the proof.

Please cite this article in press as: Dobrev VA et al. High-order curvilinear finite elements for axisymmetric Lagrangian hydrodynamics. Comput Fluids (2012), http://dx.doi.org/10.1016/j.compfluid.2012.06.004

4. Numerical results

We now present a series of numerical results using the newly developed axisymmetric curvilinear finite element formulation. For all test cases considered, we solve the global linear system for momentum conservation using a diagonally scaled conjugate

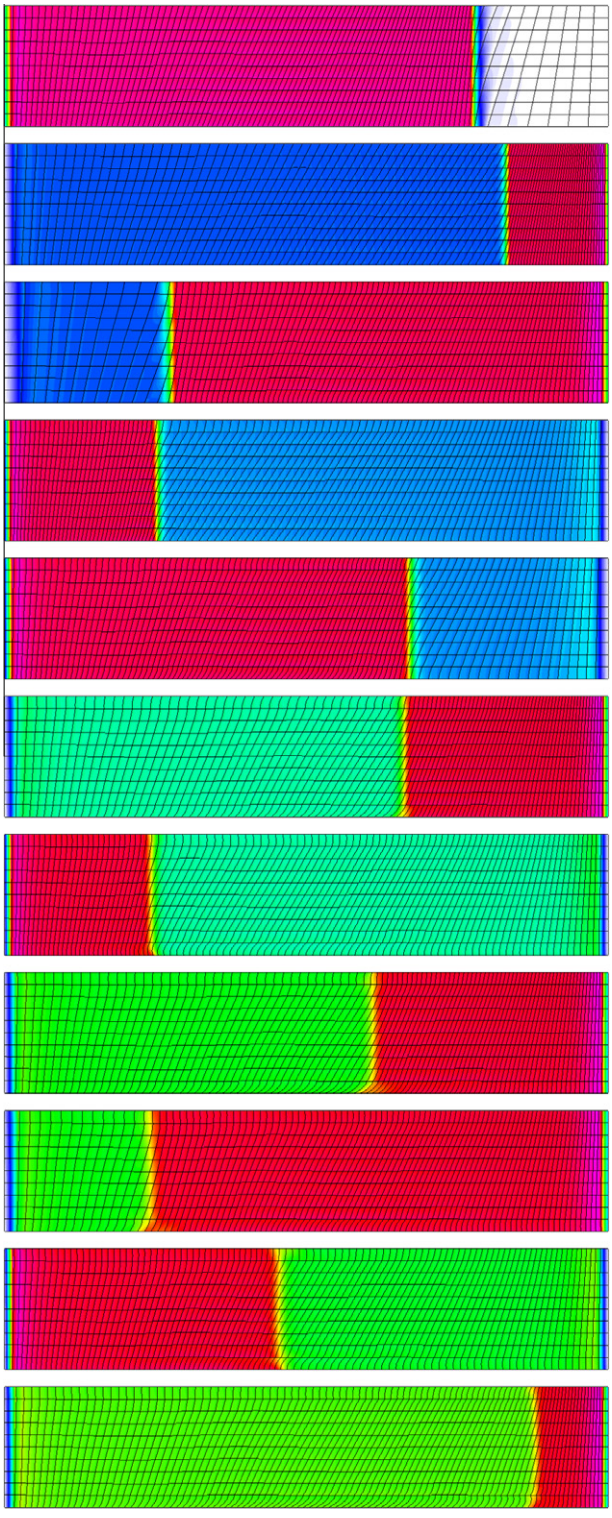

Fig. 4. Curvilinear mesh and density field sampled at multiple points per zone for the cylindrical Saltzman piston problem at $t = 0.7, 0.8, 0.88, 0.92, 0.94, 0.96, 0.975, 0.985, 0.987, 0.99$ and 0.992 for a total of 7 bounces. Each image is rescaled to an aspect ratio of 5 : 1.

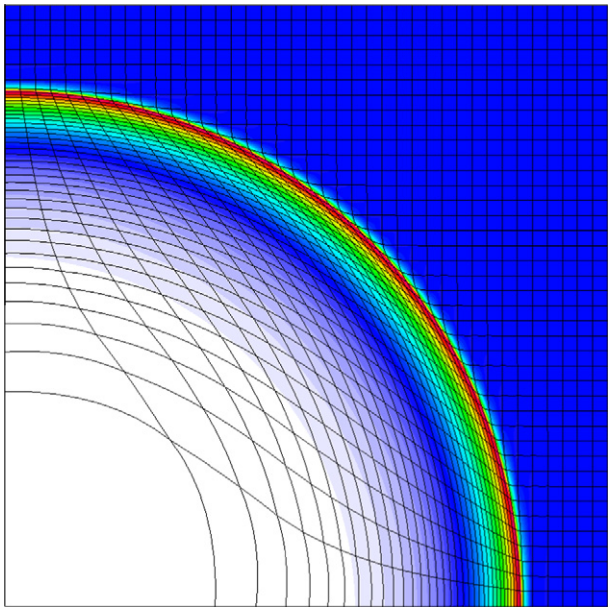

Fig. 5. Curvilinear mesh and density field sampled at multiple points per zone for the axisymmetric Sedov problem on a 40×40 Cartesian grid at time $t = 1.0$.

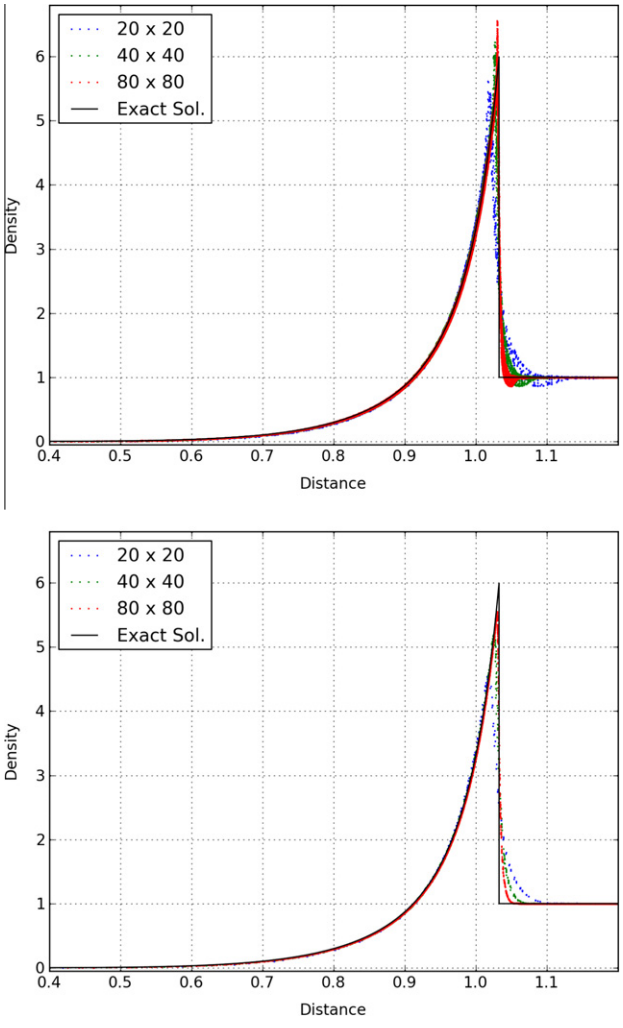

Fig. 6. Scatter plots of density vs. radius sampled at 9 points per zone (top) and 1 point per zone (bottom) for the axisymmetric Sedov problem on a Cartesian grid.

Please cite this article in press as: Dobrev VA et al. High-order curvilinear finite elements for axisymmetric Lagrangian hydrodynamics. Comput Fluids (2012), http://dx.doi.org/10.1016/j.compfluid.2012.06.004

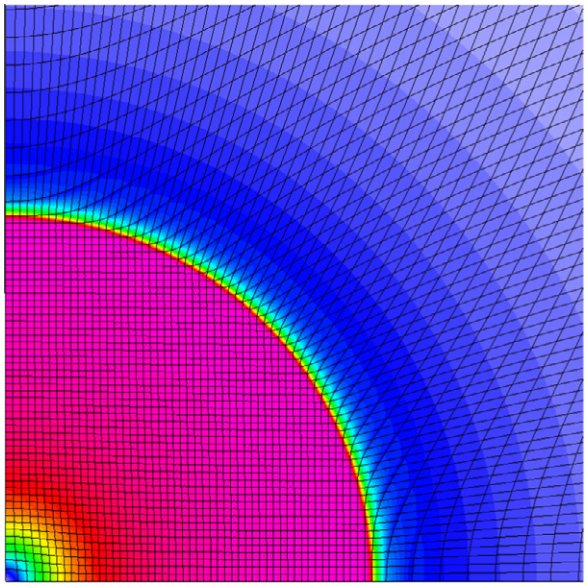

Fig. 7. Curvilinear mesh and density field sampled at multiple points per zone for the axisymmetric Noh problem on a 64×64 Cartesian grid at time $t = 0.6$.

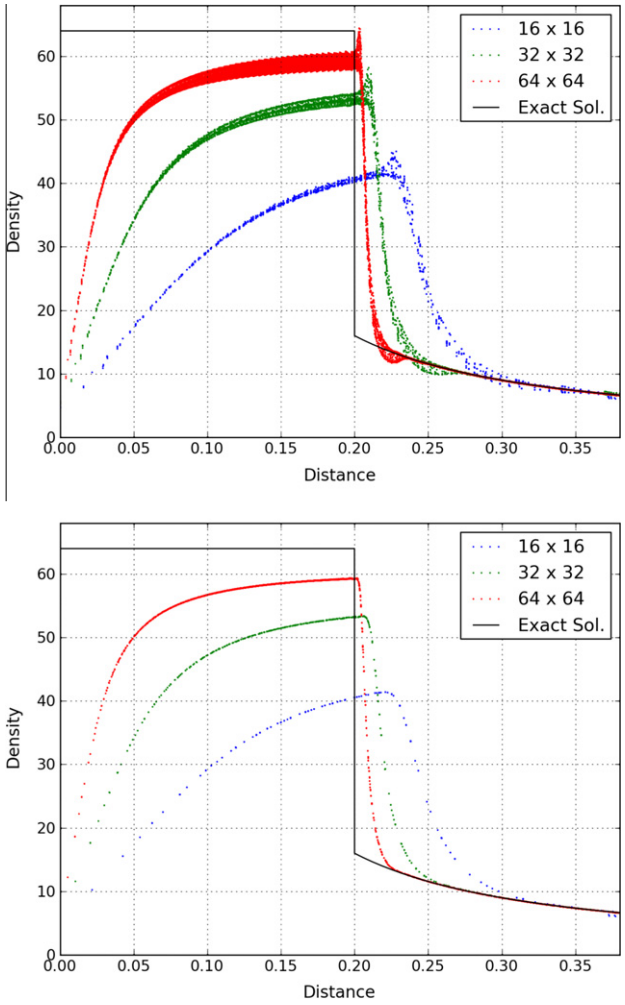

Fig. 8. Scatter plots of density vs. radius sampled at 9 points per zone (top) and 1 point per zone (bottom) for the axisymmetric Noh problem on a Cartesian grid.

gradient algorithm to a residual tolerance of 10^{-8} and unless otherwise specified, we use an ideal gas equation of state with a constant adiabatic index $\gamma = 5/3$ and the type 2 tensor artificial viscosity described in Section 3.2 with linear and quadratic coefficients $q_1 = 1/2$ and $q_2 = 2$. Furthermore, in most of these examples we only consider the use of a $Q_2 - Q_1$ method for the sake of brevity. The only exceptions are Section 4.4 where we consider a $Q_4 - Q_3$ method to demonstrate that our axisymmetric formulation is valid for arbitrary order basis functions as described in [1] and Section 4.5 where we compare against the lowest order $Q_1 - Q_0$ method. The axisymmetric $Q_2 - Q_1$ method consists of 9 kinematic degrees of freedom per zone and four discontinuous thermodynamic degrees of freedom per zone. The results in this section have been computed with our high-order finite element Lagrangian hydrocode BLAST [22], which is based on the parallel modular finite element methods library MFEM [23]. We also used the related OpenGL visualization tool GLVis [24] to plot the computed curvilinear meshes and high-order fields. In all r–z plots, the z and r axes are the horizontal and vertical axes, respectively.

4.1. Cylindrical Saltzman piston

In this test problem, a 1D piston shock wave is propagated over an initially distorted 2D mesh. The problem domain is a cylinder with $z \in [0, 1]$ and $r \in [0, 0.1]$ with initial thermodynamic conditions $\rho = 1, p = 0$ and $e = 0$. The details of how the initial skewed mesh is constructed can be found in [25]. The velocity is initially zero everywhere except at the wall $z = 0$, where a constant velocity source of $v_z = 1.0$ is applied for all time. This problem tests the ability of our axisymmetric methods to maintain a 1D planar shock front on a mesh that is not aligned with the shock flow and provides an indication of the robustness of our method with respect to mesh imprinting. It is also a good test of possible symmetry breaking near the axis of rotation.

In Fig. 4 we plot the density field and curvilinear mesh at snapshots in time corresponding to $t = 0.7, 0.8, 0.88, 0.92, 0.94, 0.96, 0.975, 0.985, 0.987, 0.99$ and 0.992. Note that the shock front has bounced from the boundary walls for a total of seven times. To our knowledge this is the latest time to which this problem has been shown to run in a purely Lagrangian manner. Note also that the shock front remains largely flat for all time and only at extremely late times do we begin to observe the minor effect of symmetry breaking near the axis of rotation.

4.2. Spherical Sedov explosion

The Sedov problem consists of an ideal gas ($\gamma = 1.4$) with a delta function source of internal energy deposited at the origin such that the total energy $E_{tot} = 1$. The sudden release of the energy creates an expanding spherical shock wave, converting the initial internal energy into kinetic energy. The delta function energy source is approximated by setting the internal energy e to zero in all degrees

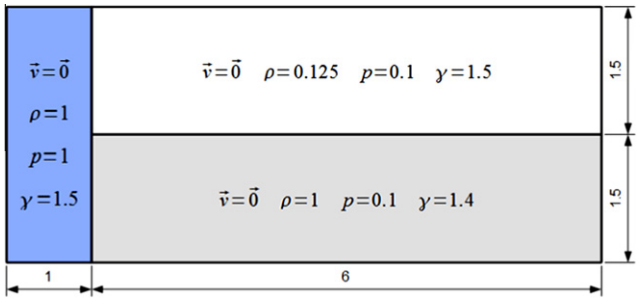

Fig. 9. Initial conditions for the axisymmetric multi-material shock triple point interaction problem.

of freedom except at the origin where the value is chosen so that the total internal energy is 1.

For this particular problem we used a finite element (discontinuous Q_1) discretization of the pressure, based on a weak variational form of the equation of state, see §2.8 in [6]. This version of the algorithm produced results with better symmetry near the origin than our default method in which the pressure is treated as a function sampled through the EOS at the quadrature points.

In Fig. 5 we plot the density field and curvilinear mesh at the final time of $t = 1.0$. In Fig. 6 we show scatter plots of the density versus the radius sampled at 9 points per zone and at 1 point per zone (at the zone center) on a sequence of refined meshes. The oscillations in the data near the shock front are at the sub-zonal level, the zone centered values do not exhibit this behavior. Note that in this calculation, the total numerical energy was conserved to machine precision for all time and we have convergence to the exact shock location, cf. Fig. 1.

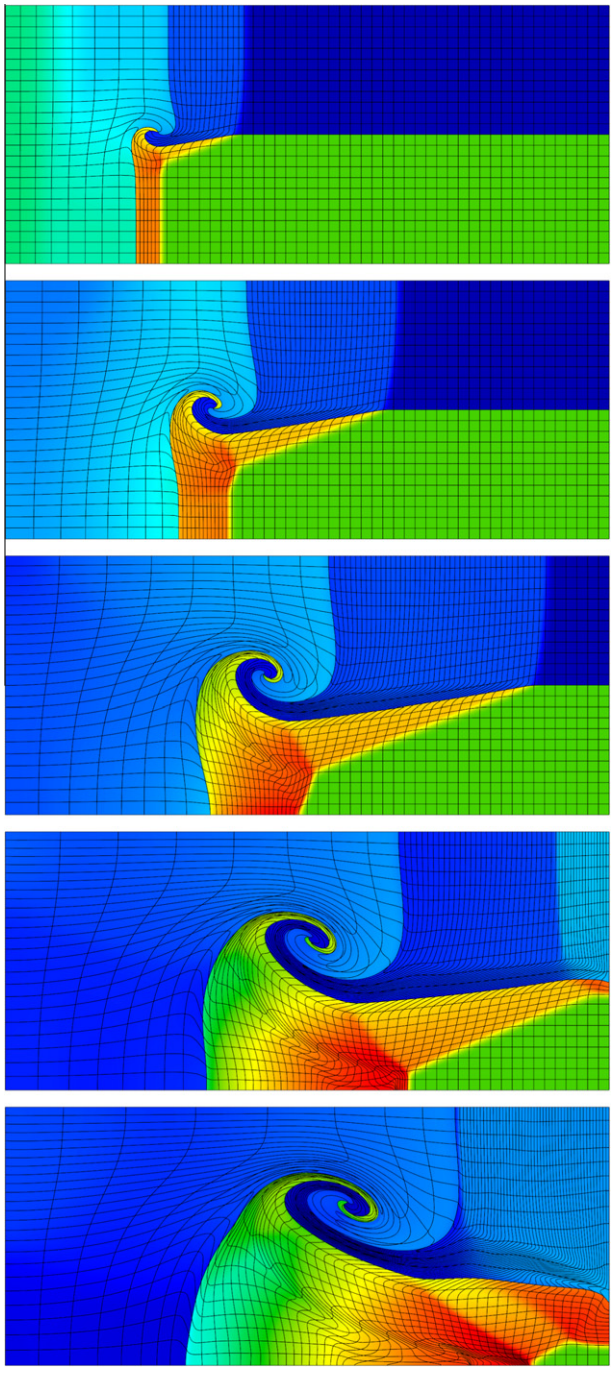

Fig. 10. Snapshots of curvilinear mesh and density field (log scale) for the axisymmetric triple point problem obtained using the $Q_4 - Q_3$ method at $t = 1, 2, 3, 4$, and 5 (top to bottom).

4.3. Spherical Noh implosion

The Noh problem consists of an ideal gas with $\gamma = 5/3$, initial density $\rho_0 = 1$ and initial energy $e_0 = 0$. The value of each velocity degree of freedom is initialized to a radial vector pointing toward the origin, $v = -\vec{r}/\|\vec{r}\|$. The initial velocity generates a spherical stagnation shock wave that propagates outward with a speed of $\frac{1}{3}$ and produces a peak post-shock density of $\rho = 64$.

In Fig. 7 we plot the density field and curvilinear mesh at the final time of $t = 0.6$. In Fig. 8 we show scatter plots of the density versus the radius sampled at 9 points per zone and at 1 point per zone (at the zone center) on a sequence of refined meshes. As with the previous problem, the oscillations in the data near the shock front are at the sub-zonal level, the zone centered values do not exhibit this behavior. Note that in this calculation, the total numerical energy was conserved to machine precision for all time.

4.4. Axisymmetric multi-material shock triple point interaction

The triple point problem describes the interaction of three materials with ideal gas equations of state. The initial domain, materials and initial conditions are shown in Fig. 9. Slip wall

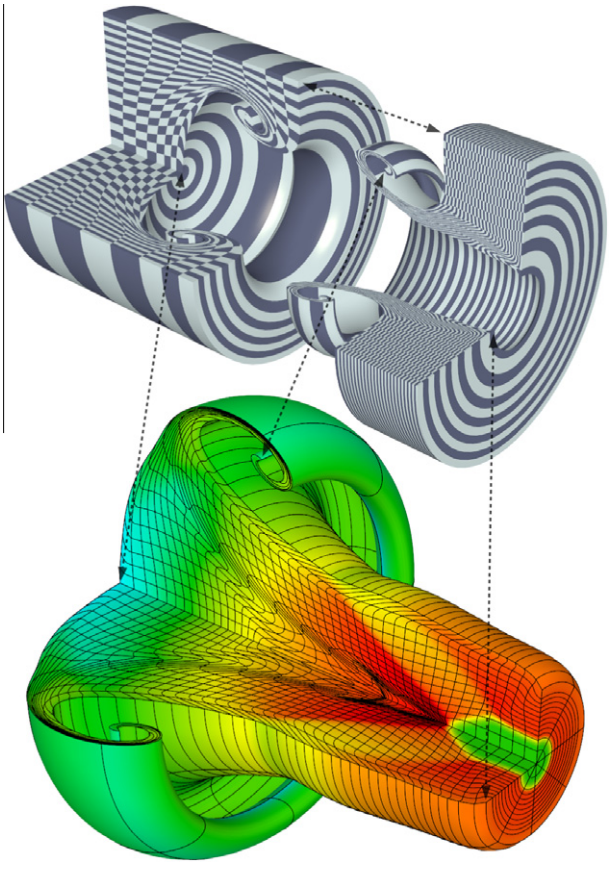

Fig. 11. Full 3D visualization of the materials in the axisymmetric triple point problem obtained using the $Q_4 - Q_3$ method at $t = 5$; revolved axisymmetric mesh (top) and density (bottom).

Please cite this article in press as: Dobrev VA et al. High-order curvilinear finite elements for axisymmetric Lagrangian hydrodynamics. Comput Fluids (2012), http://dx.doi.org/10.1016/j.compfluid.2012.06.004

boundary conditions are imposed everywhere on the boundary, i.e. $v_z = 0$ at $z = 0, z = 7$ and $v_r = 0$ at $r = 0, r = 3$.

We discretize the problem using the Q_4-Q_3 finite element space pair (see [1]) which is based on bi-quartic continuous velocity and displacement spaces (25 kinematic degrees of freedom per zone) and a bi-cubic discontinuous thermodynamic space (16 thermodynamic degrees of freedom per zone). The initial mesh is a 56×24 uniform Cartesian mesh. For all discretization parameters we use

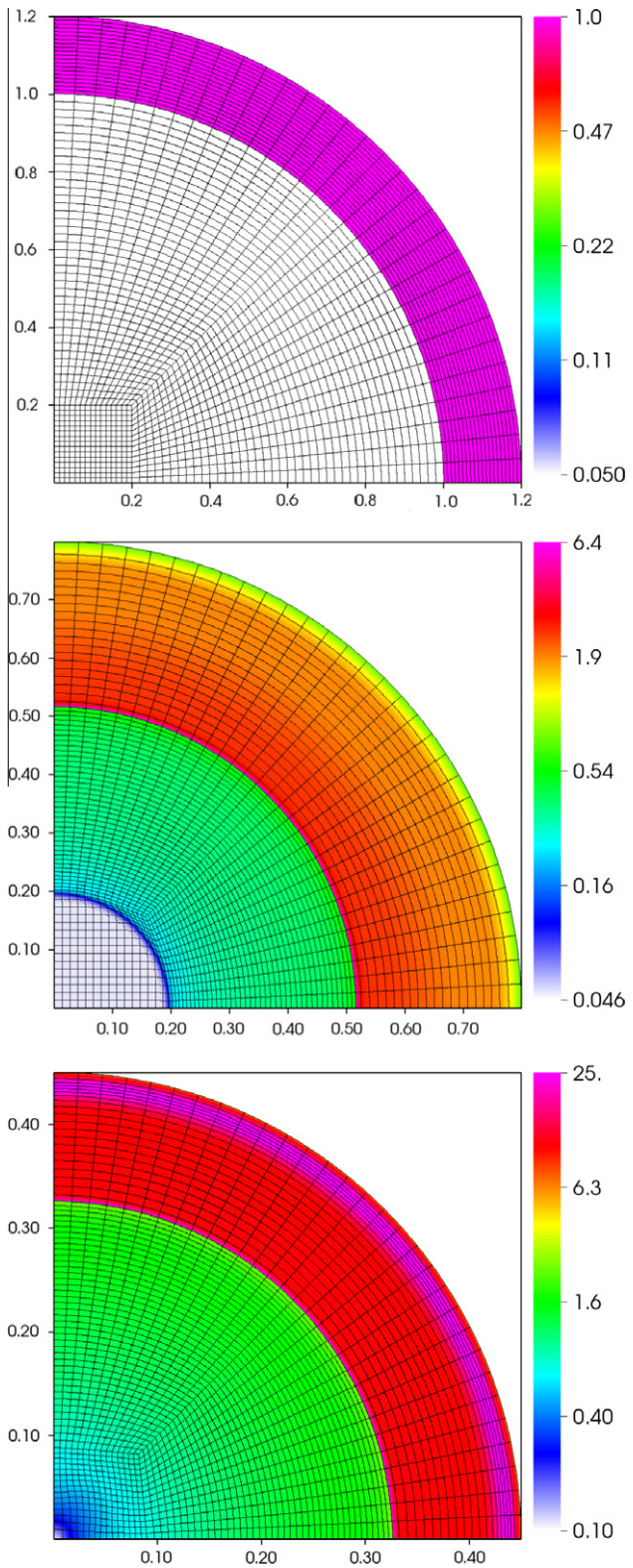

Fig. 12. Snapshots of curvilinear mesh and density field (log scale) sampled at multiple points per zone at times $t = 0, t = 0.08$ and $t = 0.15$ for the axisymmetric multi-material spherical implosion problem on an unstructured uniform mesh using the $Q_2 - Q_1$ method.

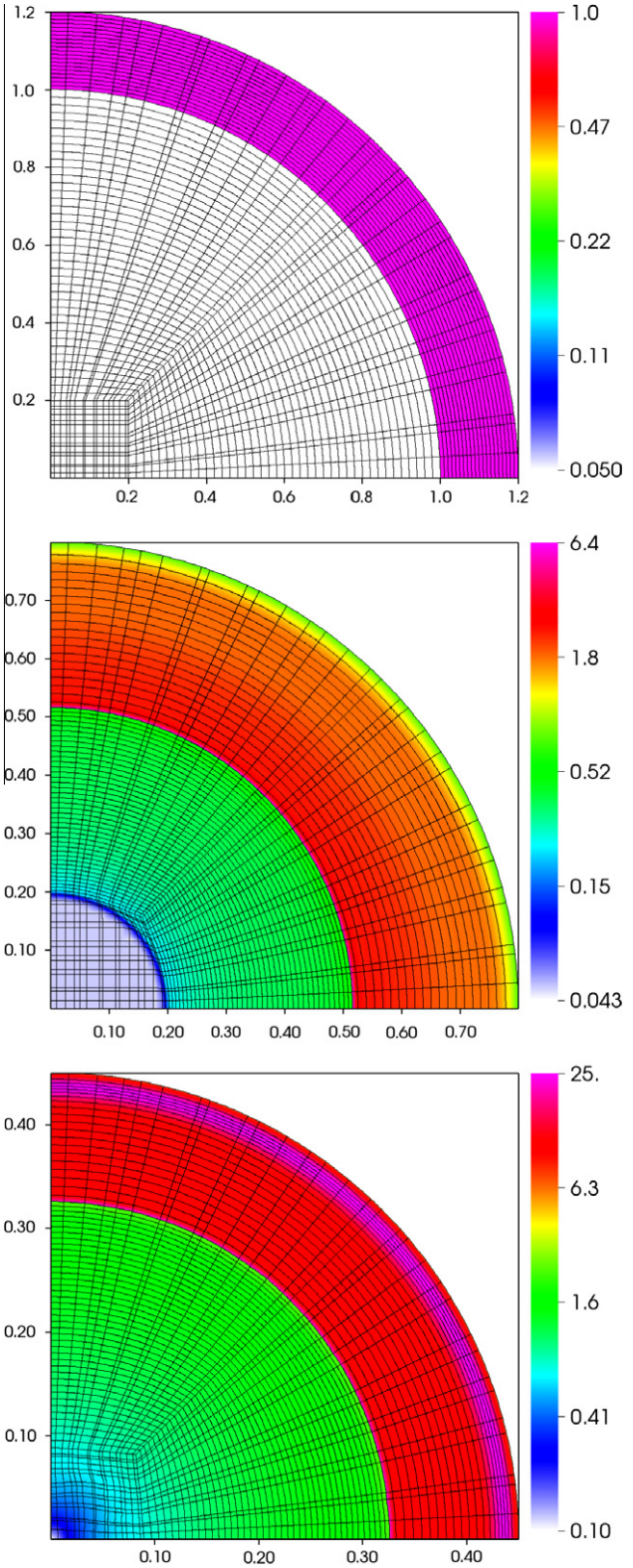

Fig. 13. Snapshots of curvilinear mesh and density field (log scale) sampled at multiple points per zone at times $t = 0, t = 0.08$ and $t = 0.15$ for the axisymmetric multi-material spherical implosion problem on an unstructured random using the $Q_2 - Q_1$ method.

Please cite this article in press as: Dobrev VA et al. High-order curvilinear finite elements for axisymmetric Lagrangian hydrodynamics. Comput Fluids (2012), http://dx.doi.org/10.1016/j.compfluid.2012.06.004

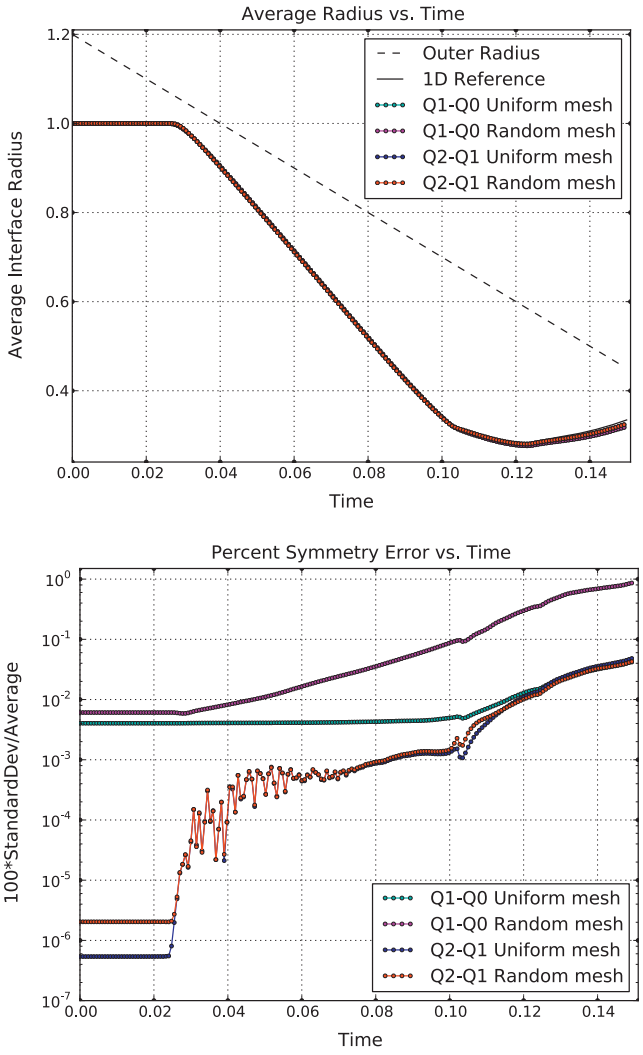

Fig. 14. Average interface radius vs. time (top) and percent symmetry error vs. time (bottom) for the axisymmetric multi-material spherical implosion problem on an unstructured uniform and random mesh, using both a $Q_1 - Q_0$ and a $Q_2 - Q_1$ method.

their default values except for the tensor artificial viscosity where we use type 4 (see [1]) modified appropriately for the axisymmetric case. For the time discretization we use the standard explicit RK4 time stepping method.

In Fig. 10, we present a sequence of snapshots of the computational mesh and density up to time $t = 5$. Note the extreme mesh distortion in the vortex region, near the horizontal material interface, and near the $r = 0$ axis. Even in the presence of such extreme deformations, our method still maintains its robustness. In Fig. 11, we plot the full 3D material domains at the final time $t = 5$ obtained by revolving the solution from the meridian cut about the axis of symmetry $r = 0$.

4.5. Multi-material spherical implosion

Here we consider a simple 1D multi-material implosion problem on unstructured 2D meshes. The problem consists of a low density material with $\rho_1 = 0.05$ in the radial range $r \in [0, 1]$ surrounded by a shell of high density material $\rho_2 = 1.0$ in the radial range $r \in [1.0, 1.2]$. Each material is at an initial pressure of $p = 0.1$ and uses an ideal gas equation of state with $\gamma = 5/3$.

This problem was originally proposed by [26] for cylindrical symmetry. Here we make a simple modification for spherical symmetry, instead of applying a time dependent pressure source to the outermost radial surface of the problem, we apply a constant velocity source of $v = -5\vec{r}/\|\vec{r}\|$. The outer surface drives a spherical shock wave inward. Ideally, the interface between the high and low density materials should remain perfectly spherical for all time due to the spherical symmetry of the velocity drive. However, the discretization errors of the initial geometry of this surface and subsequent error introduced by the numerical algorithm will be amplified over time since the interface is subject to both Richtmyer–Meshkov (RM) and Rayleigh–Taylor (RT) instabilities.

In Fig. 12 we show plots of the mesh and density on a log scale at three snapshots in time for the case of a uniform unstructured mesh. In Fig. 13 we show identical plots for the same problem on a randomly perturbed unstructured mesh. In both cases we use a $Q_2 - Q_1$ method and the initial mesh is curved by mapping all position degrees of freedom in the outer high density shell to a spherical surface. Note that the randomly perturbed mesh has both non-uniform angular spacing as well as non-uniform aspect ratios in the central "box" region. Maintaining spherical symmetry on such a mesh with a Lagrangian method is a non-trivial task, cf. Fig. 2.

In Fig. 14 we plot the average radius of the entire material interface using 5 points per edge for both cases and compare these to a reference 1D result (obtained from a high resolution 1D Lagrangian SGH calculation). We also compare to results obtained using a low order $Q_1 - Q_0$ method on refined versions of the same meshes (yielding the same total number of kinematic and thermodynamic

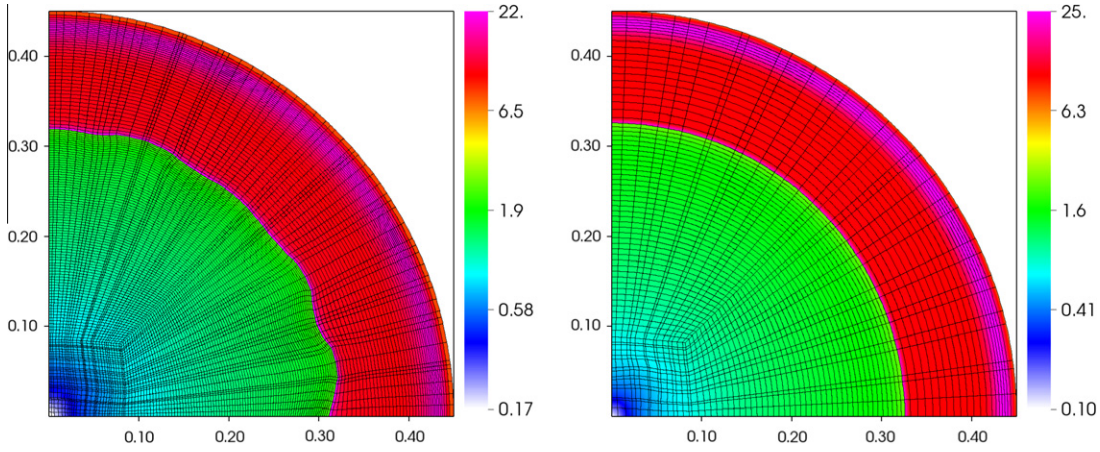

Fig. 15. Comparison of curvilinear mesh and density field (log scale) sampled at multiple points per zone at time $t = 0.15$ for the axisymmetric multi-material spherical implosion problem on an unstructured random mesh using a $Q_1 - Q_0$ method on a refined mesh (left) and a $Q_2 - Q_1$ method (right).

Please cite this article in press as: Dobrev VA et al. High-order curvilinear finite elements for axisymmetric Lagrangian hydrodynamics. Comput Fluids (2012), http://dx.doi.org/10.1016/j.compfluid.2012.06.004

degrees of freedom) with 3 plot points per edge (yielding the same total number of interface plot points). For the $Q_2 - Q_1$ case, each mesh yields essentially identical results in the average radius and both are in good agreement with the 1D high resolution reference solution. In addition, the $Q_2 - Q_1$ values are in better agreement with the reference solution than the $Q_1 - Q_0$ values. In Fig. 14 we also plot the normalized standard deviation of this radial surface which indicates the symmetry error over time. For all cases, we observe a sharp rise in symmetry error as the shock first passes over the interface around $t = 0.03$ and impulsively accelerates it, due to the RM instability. As the shell begins to decelerate due to multiple shock reflections from the origin around $t = 0.11$, the interface is subject to RT instability an we observe another sharp increase in symmetry error. The $Q_2 - Q_1$ method is significantly better at preserving the interface symmetry on the random mesh with errors less than 0.1% at the final time of $t = 0.15$, more than an order of magnitude less than the $Q_1 - Q_0$ method, which can be clearly seen in the comparison plots of Fig. 15.

5. Conclusions

In this paper we presented an extension of our high-order curvilinear finite element method for solving the equations of compressible hydrodynamics in a Lagrangian frame to the case of axisymmetric problems. This extension results in relatively simple modifications to the semi-discrete formulation, consisting of a rescaled momentum conservation equation and new radial terms in the pressure gradient and artificial viscosity forces, and was shown to exactly conserve total numerical energy. We also demonstrated via numerical examples the benefits of the new high order curvilinear axisymmetric discretization method, including: significant improvements in symmetry preservation for symmetric flows even when the underlying mesh is highly non-uniform; the ability to more accurately capture geometrical features of a flow region and maintain robustness with respect to mesh motion using curvilinear zones and high order bases; sharper resolution of the shock front for a given mesh resolution; and a substantial reduction in mesh imprinting for shock wave propagation not aligned with the computational mesh.

Acknowledgments

This work performed under the auspices of the US Department of Energy by Lawrence Livermore National Laboratory under Contract DE-AC52-07NA27344, LLNL-JRNL-521372.

References

[1] Dobrev VA, Kolev TzV, Rieben RN. High order curvilinear finite element methods for Lagrangian hydrodynamics. SIAM J Sci Comput, submitted for publication.
[2] Ockendon H, Ockendon J. Waves and compressible flow. Texts in applied mathematics, vol. 47. Springer-Verlag; 2004.
[3] Benson DJ. Computational methods in Lagrangian and Eulerian hydrocodes. Comput Methods Appl Mech Eng 1992;99:235–394.
[4] Zel'dovich YaB, Raizer YuP. Physics of shock waves and high-temperature hydrodynamic phenomena. New York: Academic Press; 1967.
[5] Castor J. Radiation hydrodynamics. Cambridge, UK: Cambridge University Press; 2004.
[6] Dobrev VA, Ellis TE, Kolev TzV, Rieben RN. Curvilinear finite elements for Lagrangian hydrodynamics. Int J Numer Methods Fluids 2010;65(11–12):1295–310.
[7] Wilkins ML. Methods in computational physics, vol. 3. Academic Press; 1964 [chapter Calculation of elastic–plastic flow].
[8] Whalen P. Algebraic limitations on two dimensional hydrodynamics simulations. J Comput Phys 1996;124(1):46–54.
[9] Caramana EJ, Burton DE, Shashkov MJ, Whalen PP. The construction of compatible hydrodynamics algorithms utilizing conservation of total energy. J Comput Phys 1998;146:227–62.
[10] Margolin L, Shashkov M. Using a curvilinear grid to construct symmetry-preserving discretizations for Lagrangian gas dynamics. J Comput Phys 1999;149:389–417.
[11] Barlow A. A compatible finite element multi-material ALE hydrodynamics algorithm. Int J Numer Methods Fluids 2007;56:953–64.
[12] Scovazzi G, Christon MA, Hughes TJR, Shadid JN. Stabilized shock hydrodynamics: I. A Lagrangian method. Comput Methods Appl Mech Eng 2007;196(4–6):923–66.
[13] Scovazzi G, Love E, Shashkov M. Multi-scale Lagrangian shock hydrodynamics on Q1/P0 finite elements: theoretical framework and two-dimensional computations. Comput Methods Appl Mech Eng 2008;197:1056–79.
[14] Lipnikov K, Shashkov M. A framework for developing a mimetic tensor artificial viscosity for Lagrangian hydrocodes on arbitrary polygonal meshes. J Comput Phys 2010;229(20):7911–41.
[15] Matejovic P, Adamik V. A one-point integration quadrilateral with hourglass control in axisymmetric geometry. Comput Methods Appl Mech Eng 1988;70(3):301–20.
[16] Matejovic P. Quadrilateral with high coarse-mesh accuracy for solid mechanics in axisymmetric geometry. Comput Methods Appl Mech Eng 1991;88(2):241–58.
[17] Maire P-H. A high-order cell-centered Lagrangian scheme for two-dimensional compressible fluid flows on unstructured meshes. J Comput Phys 2009;228(7):2391–425.
[18] Maire P-H. A high-order cell-centered Lagrangian scheme for compressible fluid flows in two-dimensional cylindrical geometry. J Comput Phys 2009;228:6882–915.
[19] Sedov LI. Similarity and dimensional methods in mechanics. 10th ed. CRC Press; 1993.
[20] Burton DE. Multidimensional discretizations of conservation laws for unstructured polyhedral grids. Technical report UCRL-JC-118306. Lawrence Livermore National Laboratory; 1994.
[21] Caramana EJ, Shashkov MJ. Elimination of artificial grid distortion and hourglass-type motions by means of Lagrangian subzonal masses and pressures. J Comput Phys 1998;142(2):521–61.
[22] BLAST: high-order finite element Lagrangian hydrocode. <http://www.llnl.gov/CASC/blast>.
[23] MFEM: modular parallel finite element methods library, <http://mfem.googlecode.com>.
[24] GLVis: OpenGL visualization tool. <http://glvis.googlecode.com>.
[25] Dukowicz JK, Meltz BJ. Vorticity errors in multidimensional lagrangian codes. J Comput Phys 1992;99(1):115–34.
[26] Galera S, Maire P-H, Breil J. A two-dimensional unstructured cell-centered multi-material ALE scheme using VOF interface reconstruction. J Comput Phys 2010;229(16):5755–87.

Please cite this article in press as: Dobrev VA et al. High-order curvilinear finite elements for axisymmetric Lagrangian hydrodynamics. Comput Fluids (2012), http://dx.doi.org/10.1016/j.compfluid.2012.06.004